



# Shape and surface property effects on displacement enhancement by nanoparticles

Xukang Lu, Moran Wang<sup>\*</sup>

Department of Engineering Mechanics, Tsinghua University, Beijing 100084, China

## ARTICLE INFO

### Keywords:

Nanoparticle  
Shape  
Surface property  
Multiphase displacement  
Interfacial adsorption  
Microfluidics

## ABSTRACT

This work studies the mechanisms of shape and surface property effects on multiphase displacement enhancement by nanoparticle suspensions in porous media. Three representative nanoparticles with promising industry applications, namely silica nanoparticles, graphene oxide and hydroxylated carbon nanotubes have been considered comprehensively. The correspondence between particle shape and surface property, interfacial adsorption behaviors, and displacement patterns has been analyzed systematically. Significant differences in adsorption tendencies and consequences are revealed via adsorption characterizations with theoretical derivations and microscopic modeling. For liquid–liquid interfacial adsorption, sheet-like and fibrous shapes with amphiphilicity are more beneficial to adsorption and retention at interface, which promotes dynamic interfacial tension reduction and emulsion stabilization. For solid surface adsorption, spherical and fibrous shapes with hydrophilicity are more favorable for formation of nanoscale rough structures, which induces the development and maintenance of wetting films. Visualization and quantification of multiphase displacement in complex structures via microfluidic experiments enable us to evaluate the relative performances and unravel displacement enhancement modes. Hydroxylated carbon nanotubes exhibit optimal performance, followed by graphene oxide and then silica nanoparticles, with clear distinction in interfacial phenomena. Enhanced liquid–liquid interfacial adsorption behaviors result in the invasion into un-swept regions with sweeping efficiency enhancement, whereas enhanced solid surface adsorption behaviors drive the detachment of defending phase in the form of isolated ganglia.

## 1. Introduction

Multiphase displacement in porous media is ubiquitous in many natural and industrial scenarios, such as hydrocarbon recovery [1], carbon dioxide sequestration [2], groundwater and soil remediation [3], and biomedical research [4]. Chemical flooding, which adds chemical reagents into the injected fluid, shows remarkable displacement enhancement effects with significant impacts on multiphase interactions [5–10]. The application of nanoparticles has drawn much attention in recent years due to their ultra-small size, interfacial properties, thermal and mechanical strength, and environmental friendliness [11–16]. However, the performance and mechanism of displacement enhancement by nanoparticle suspensions are still under debate.

It has been widely reported that nanoparticle adsorption onto the solid surface will induce wettability alternation. Dehghan et al. analyzed the thermodynamics and kinetics of the adsorption process of silica nanoparticles onto calcite [17]. Al-Ansari et al. performed adsorption

experiments using silica nanoparticles and observed a wettability shift from oil-wet to water-wet [18]. Similar effects were also detected in other research using metal oxide nanoparticles [19], graphene oxide [20], and functionalized carbon nanotubes [21]. The in-situ observations during microfluidic experiments verified the wetting state variation [20,22]. However, microscopic interpretations from solid surface adsorption to wetting behaviors remain unclear.

Liquid–liquid interfacial adsorption may reduce interfacial tension (IFT) or stabilize emulsions/foams. Xu et al. investigated nanoparticles' role in mobilizing trapped oil droplets in single pore-throat geometries [23]. They concluded that silica nanoparticles serve as a weak surfactant to increase the capillary number. Tajik et al. reported that silica-graphene nanohybrid can achieve up to a two-thirds reduction in IFT with crude oil and verified displacement enhancement by micro-model tests [24]. Preparation of Pickering emulsions has also been adopted to characterize the interfacial property of nanoparticles [24–26]. However, the relationship between liquid-liquid interfacial

<sup>\*</sup> Corresponding author.

E-mail address: [mrwang@tsinghua.edu.cn](mailto:mrwang@tsinghua.edu.cn) (M. Wang).

<https://doi.org/10.1016/j.ijmecsci.2023.108471>

Received 28 February 2023; Received in revised form 27 April 2023; Accepted 16 May 2023

Available online 17 May 2023

0020-7403/© 2023 Elsevier Ltd. All rights reserved.

adsorption and enhanced displacement mode has not been fully understood.

Particle ordering in the three-phase contact region has been demonstrated to produce excess structural disjoining pressure separating the interfaces. Extensive efforts have been made to reveal the mechanism from particle ordering and structure transition to non-wetting phase detachment [27,28]. Displacement experiments showed additional recovery using silica and polymeric nanoparticle suspensions, but under strongly water-wet states with low IFT [29,30]. Besides, high particle concentration, small particle size and ideal monodispersity are the premises for the significance of excess disjoining pressure, which are usually hard to achieve for common experimental and field conditions [1,31].

Shape and surface property are two fundamental factors in nanomaterial selection and design [32–37]. The commonly used inorganic nanomaterials include silica, metal oxide, and carbon [1]. Silica and metal oxide nanoparticles are usually spherical or near-spherical with hydrophilic nature. Low-dimensional carbon materials, such as graphene oxide and functionalized carbon nanotubes, are non-spherical with amphiphilic nature. Strongly hydrophobic nanoparticles cannot be well-dispersed in water without additives, which is out of the scope here. The surface property can also be tuned by surface modifications and coatings [38–41]. Due to the complexity and multiscale feature of multiphase displacement by nanoparticle suspensions, the differences between typical nanoparticles and the influence of material properties have not been well explored by experiments. Only a few comparative studies have been conducted to evaluate the relative performances [42–45]. Nazari et al. compared wettability alternation effects of eight kinds of nanoparticles [42]. Silica and calcium carbonate nanoparticles were found to achieve the highest oil recovery in spontaneous imbibition tests and core flooding experiments. Alomair et al. compared silica, metal oxide nanoparticles and their mixtures also by core flooding experiments [43]. They claimed that a mixture of silica and aluminum oxide should be the best candidate for displacement enhancement. The abovementioned evaluations noted differences in nanoparticle performances without clarification of the influencing mechanism of material properties. Strict control of suspension compositions and environmental conditions is also lacking. Therefore, it is necessary to shed further light on how shape and surface property of nanomaterials manipulate displacement enhancement effects.

Microfluidics provides a powerful tool to understand multiphase displacement in porous media [46,47]. Real-time visualization and repeatability pave the way for comparative study and mechanism analysis. Advances in constructing realistic porous structures onto microchips, such as reservoir-on-a-chip [48,49], soil-on-a-chip [50], and coreflood-on-a-chip [51], enhance the reliability of results. Combination of macroscopic observations and microscopic interpretations makes it possible to establish the relationship between shape and surface property, interfacial adsorption behaviors, and displacement patterns.

In this work, we selected three representative nanoparticles, namely silica (spherical and hydrophilic), graphene oxide (sheet-like and amphiphilic) and hydroxylated carbon nanotubes (fibrous and amphiphilic) for systematic comparison. The natural abundance and accessibility of the selected materials with unique properties provide them with the most promising application potential [1,13]. Suspensions were prepared under similar conditions with reliable stability. Interfacial tension measurements, emulsification tests and detachment energy derivations demonstrate differences in liquid–liquid interfacial adsorption. Surface morphology characterization, curvature distribution analysis and film transition modeling reveal differences in solid surface adsorption. Influence of particle shape and surface property was determined based on the above analysis. Displacement experiments on microfluidic chips with complex porous structures were conducted to evaluate their relative performances. By combining quantification of displacement efficiency, visualization of pore-scale phenomena and statistics of topological information, we clarified typical enhanced

displacement modes consistent with microscopic adsorption behaviors. Our findings help elucidate the physics underlying displacement enhancement by nanoparticle suspensions.

The structure of this paper is as follows. In Section 2, the materials and experimental methods are introduced. Section 3 presents the results of adsorption characterizations and displacement experiments. Mechanism analysis explains the consistency of adsorption behaviors and displacement modes and unravels the role of particle shape and surface property. Finally, the conclusions are drawn in Section 4.

## 2. Materials and experimental methods

In this section, the selection and preparation of nanoparticle suspensions, procedures of parameter characterizations, experimental design and methodology for adsorption behaviors, microfluidic chip design and fabrication, and microfluidic experimental setup were introduced.

### 2.1. Selection and preparation of nanoparticle suspensions

Silica ( $\text{SiO}_2$ ) nanoparticles can be divided into silica sols and fumed silica according to the synthesis method. Silica sols, prepared by hydrolysis and condensation in silicate solutions, can maintain monodisperse and spherical at high concentrations. The presence of rich silanol groups makes them strongly hydrophilic. Graphene oxide (GO) is synthesized through the oxidation of graphite flakes using modified Hummers' method [52]. GO nanosheets have been known to be dispersible in water attributed to the hydrophilic functional groups. The coexistence of hydrophilic sites at the edge and the hydrophobic basal plane makes GO naturally amphiphilic [53]. Carbon nanotubes (CNT) are fibrous but non-dispersible in water. Functionalized CNT exhibits similar surface property to GO by inserting functional groups on the sidewall of CNT [54].

The stock silica sol (Alfa Aesar) was diluted with deionized (DI) water to prepare the suspension. Powders of graphene oxide nanosheets (Macklin) and hydroxylated multiwalled carbon nanotubes (Timesnano) were dispersed in DI water and stirred at 800 rpm for 30 min. The concentration was controlled at 0.2 wt% for all cases. Strong sonication using an ultrasound probe has been conducted for 15–60 min under ice-water bath to ensure their dispersity. To clarify the performance and mechanism of nanoparticles themselves, no additives such as surfactants were involved and all environmental parameters were kept similar for brine and nanoparticle suspensions. The pH value was controlled using 1 M NaOH/HCl, and the salinity was adjusted using NaCl. For the simplicity of expression, in the following text the three kinds of nanoparticles will be referred to as  $\text{SiO}_2$ , GO and CNT-OH.

### 2.2. Particle and suspension characterizations

The particle size distribution and zeta potential were measured by dynamic light scattering (DLS) using a Zetasizer Nano-ZS (Malvern Instruments, UK). Morphology and also characteristic sizes of the materials were characterized via transmission electron microscopy (JEM-2010 TEM, JEOL, Japan). The TEM samples were prepared by placing a droplet of the suspension onto the copper mesh and then dried for observations.

Information of the surface functional groups was obtained by Fourier transform infrared spectroscopy (FTIR) analysis with a X70 spectrometer (Netzsch, Germany). We further evaluated the surface wettability of nanomaterials by depositing nanoparticles onto clean substrates and measuring aqueous contact angles on the formed particle layer following the procedures described in Section 2.3. Considering the surface roughness, the obtained results only serve as an estimation of the material wettability.

The rheology tests were performed using a rotational rheometer (Haake Mars III, Thermo Fisher Scientific, USA) equipped with a coaxial

cylinder geometry (CC25 DIN Ti) at 25 °C.

### 2.3. Interfacial parameter measurements

Interfacial parameters were characterized using a Drop Shape Analyzer (DSA 25, Krüss, Germany). Contact angle measurements were performed by placing a droplet of the suspension onto the quartz substrate submerged in a decane-filled reservoir. Before each experiment, all substrates were ultrasonically cleaned with acetone, absolute ethanol and DI water for ten minutes sequentially, then dried and immersed in the oil-filled reservoir. The aqueous contact angle was determined using Young-Laplace fitting method and recorded until a relatively stable state was reached (contact angle change less than 1° per hour). The above measurements are to characterize intrinsic wettability conditions for nanoparticle suspension/decane/quartz systems. Interfacial tension (IFT) measurements were performed using the pendant drop method. Dynamic IFT effect can be captured by changing the needle injection rate and droplet pending time until equilibrium.

### 2.4. Emulsification tests

Equal volumes of aqueous phase and decane were added to test tubes and mixed using a homogenizer at a speed of 5000 rpm for 5 min. The samples were standing for one week to evaluate the stability of nanoparticle adsorption. The inner structure of the Pickering emulsions was then characterized via an inverted microscope (Nikon Ti2).

### 2.5. Solid surface adsorption characterizations

Nanoparticle adsorption onto the solid surface was investigated by the following procedures. Firstly, clean quartz substrates were immersed in suspensions for 4 h, which is long enough for reaching a saturated state [55] and also consistent with the time scale for the microfluidic experiments. Secondly, the substrates were flushed with DI water before drying with nitrogen to remove the unadsorbed nanoparticles and other components in the suspension, which ensures that the measured surface texture change was induced by spontaneous adsorption rather than deposition during solvent evaporation. Finally, atomic force microscopy

(Dimension Icon AFM, Bruker, USA) was utilized to characterize the surface morphology of the substrates after adsorption.

### 2.6. Microfluidic chip design and fabrication

The microfluidic chip was constructed based on a multi-step reservoir-on-a-chip design paradigm [49]. The porous medium was regenerated by a two-step QSGS algorithm based on microstructure information from real rock samples (Changqing oil field, China), which yields hierarchical characteristics and wide pore size distribution similar to realistic porous media (Fig. 1(a)).

The microchips were made from silicon wafers considering the small and dense pore geometries. The fabrication procedure includes image import into AutoCAD, standard photolithography, and inductively coupled plasma–deep reactive ion etching (ICP-DRIE) [56]. The wafer was heated to 1000 °C under oxygen after etching to create a uniform silicon dioxide layer with wettability similar to that of a quartz surface. The patterned wafer was then anodically bonded to the Pyrex glass wafer (Schott). The upstream and downstream of the porous structure were drilled with 2 mm diameter holes for the inlet and outlet.

We also performed batch experiments on oil-wet surfaces under the same conditions to investigate the influence of substrate property and confirm differences in displacement enhancement modes. The wafers were washed with dilute hydrochloric acid and dichlorodimethylsilane, and then put in the fume hood for 24 h to keep the hydrophobic condition.

A more heterogenous structure with an artificial preferential flow pathway (PFP) was constructed to discuss the influence of flow heterogeneity [9,57]. The repeatable PFP was realized by adding a parallel high-permeability zone to the same matrix structure and changing the injection method as shown in Fig. 1(b). In the following text the two porous structures will be referred to as Matrix and PFP, respectively.

### 2.7. Microfluidic experimental setup

The microfluidic experimental setup is shown in Fig. 1(d). The cleaned microchip was fixed by a custom-designed fixture under the fluorescence microscope (Nikon SMZ18) after treated in a vacuum for

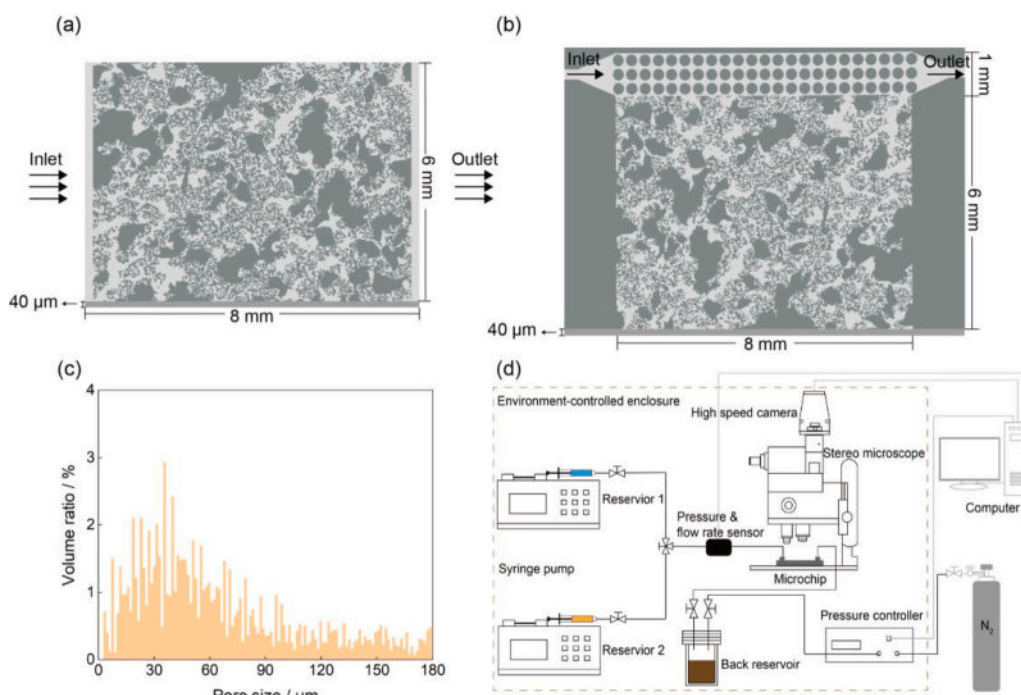


**Fig. 1.** Microchip design and experimental setup. (a) and (b) show the geometry and appearance of the Matrix and PFP microchip structures. The lighter part is the flow channel and the darker part is the solid phase. (c) Pore size distribution of the regenerated porous media. The 2D pore size distribution ranges from 2 μm to 180 μm, and the corresponding 3D hydraulic diameter ranges from 4 to 65 μm. (d) Schematic diagram of the experimental setup. The microfluidic system consists of a microchip, a fluorescence microscope, syringe pumps (Harvard Pump 11 Elite), syringes (Hamilton), a pressure controller (Fluigent, MFCS-8C), a flow rate sensor (Fluigent, FRP), a pressure sensor (Elveflow, MSR), and an image processing server. Reservoir 1, Reservoir 2 and back reservoir correspond to the invading fluid, defending fluid and back collector under controlled pressure, respectively.

12 h. The fluorescent dyed oil (100 ppm Nile Red in decane) in Reservoir 2 was injected as the defending fluid until the entire pore space was filled. The bandpass wavelengths of the filter are selected to match the fluorescent peak excitation and emission wavelengths of Nile Red dissolved in oil. The valve was then switched to Reservoir 1 and the invading fluid was injected at a constant flow rate. The characteristic capillary number was controlled at approximately  $2.6 \times 10^{-6}$ , which is consistent with previous pore-scale studies and practical conditions [58, 59]. The waste liquid was collected in the back reservoir under atmospheric pressure. The displacement process lasted until a changeless phase distribution (saturation change less than 1% per 10 PV injection) was reached. Each experiment was repeated to ensure the reliability of the displacement performance.

## 2.8. Image processing and analysis

Image processing was performed using a self-developed algorithm based on the Image Processing Toolbox of Matlab. The fluorescent signal intensity of the dyed defending fluid is much higher than other phases, with signal-to-noise ratio  $> 10$ . The real-time RGB images with a time resolution of 1 s were converted into binary form. A threshold value can be unambiguously determined for each image. Gamma correction and noise filtering were also conducted to ensure image quality. Phase distribution can be determined by picture subtraction from the initial time. The invading phase saturation or the displacement efficiency is defined as  $S = (S_0 - S_r)/S_0$ , where  $S_0$  is the initial defending phase volume and  $S_r$  is the defending phase volume at a given time. Topological analysis was

further performed to capture the evolution of flow patterns. By identifying residual ganglia of the defending phase, we calculated volume fraction of larger clusters (accounting for more than 1% of the total volume)  $V_1$  and oil ganglion number  $N_g$ .

## 3. Results and discussion

In this section, experimental results and mechanism analysis were presented. Differences in shape and surface property lead to differences in particle adsorption behaviors. Performances in IFT reduction and emulsion stabilization reflect liquid-liquid interfacial adsorption tendencies, which are further confirmed by deriving the particle detachment energy. Surface texture and curvature distribution changes demonstrate solid surface adsorption consequences, which are further investigated by modeling the wetting film transition. In microfluidic experiments, phase distribution evolutions are quantified and analyzed. Typical displacement enhancement modes are determined from pore-scale observations and verified by topological analysis. Influences of heterogeneity and substrate property of the porous media are also discussed.

### 3.1. Suspension property

Fig. 2 demonstrates the morphology and surface chemistry of the three nanomaterials. TEM micrographs (Fig. 2(b)) showed their distinct differences in particle shapes and thereby characteristic sizes. As shown in Fig. 2(c), FTIR spectra displayed similar adsorption peaks at

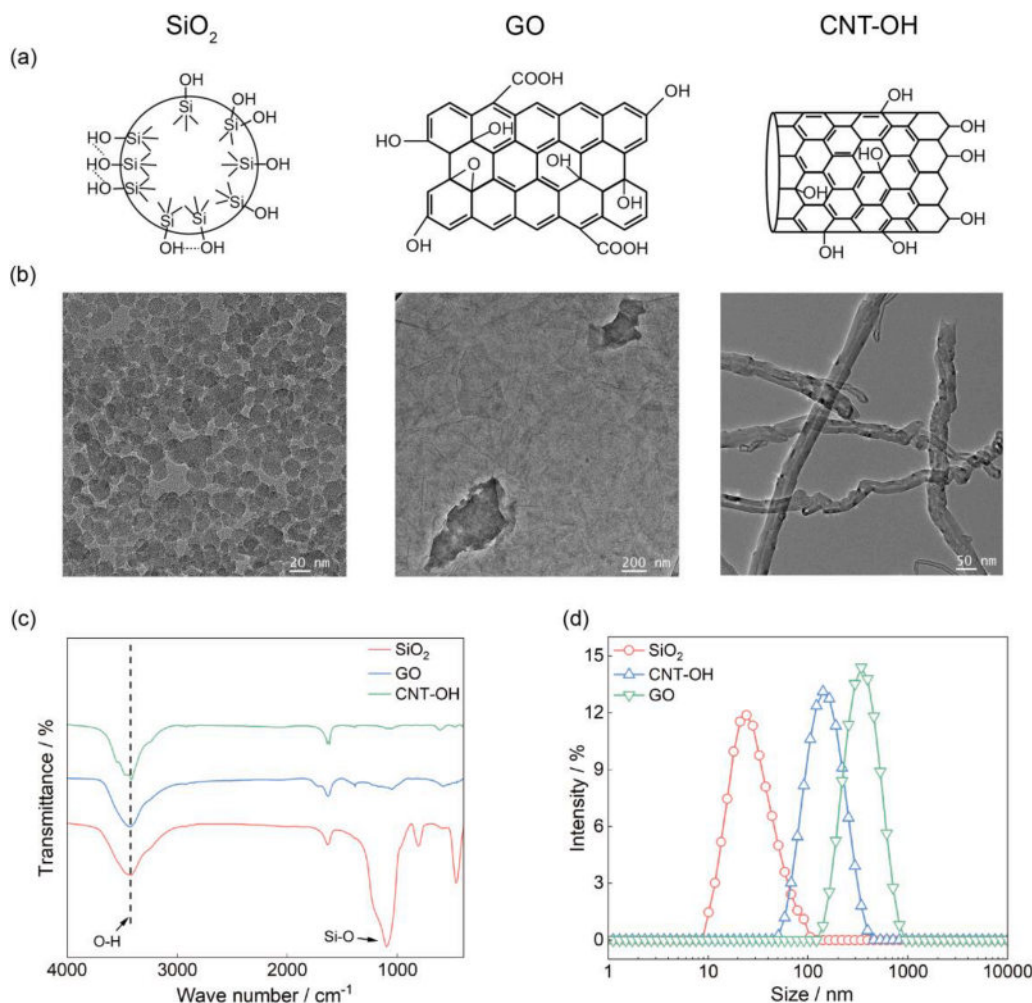


**Fig. 2.** Schematic and characterizations of nanoparticle suspensions. (a) Schematic of the shapes and surface properties of SiO<sub>2</sub>, GO and CNT-OH. (b) TEM graphs of nanoparticles showing their morphology and size. (c) DLS characterization of the particle size distribution. DLS results confirmed the suspension stability, while the measured hydraulic diameters of GO and CNT-OH were inaccurate due to their large aspect ratio. (d) FTIR spectra of the three nanomaterials. Hydroxyl groups were detected as the major functional groups with hydrophilicity.

approximately  $3400\text{--}3450\text{ cm}^{-1}$ , attributed to the stretching vibration of O—H in hydroxyl groups. The hydroxyl groups are the main origin of hydrophilicity, whereas the hydrophobic polyaromatic islands of unoxidized benzene rings of GO and CNT-OH lead to their amphiphilicity, which has also been reflected in material wettability characterizations (Table S.1). The prepared suspensions remained well-dispersed with a unimodal size distribution after 24 h, as presented in Fig. 2(d). Rheology measurements indicated that the suspensions are all Newtonian fluids with insignificant change in viscosity (Table S.1), while GO and CNT-OH yielded slightly higher viscosity than  $\text{SiO}_2$ . More details of the nanomaterial and suspension properties can be found in Table S.1.

### 3.2. Wettability change

Fig. 3 presents contact angle variations under different conditions. The brine composition also induced a non-negligible wettability change, which is sometimes ignored in previous studies. Excluding pH and salinity effects, nanoparticles were found to further decrease the aqueous-phase contact angle to varying degrees. CNT-OH suspension yielded the largest contact angle reduction, followed by GO and then  $\text{SiO}_2$ . On the one hand, the maximum contact angle change was less than  $15^\circ$  compared to brine and all cases were under moderately water-wet conditions. According to our previous research, such contact angle variations should have a minor impact on displacement efficiency [57]. On the other hand, contact angle is a comprehensive parameter that related to both liquid-liquid and solid-liquid interfacial properties. Therefore, the difference in contact angle changes suggests that CNT-OH should have a stronger ability to influence the interfacial properties.

### 3.3. Liquid-liquid interfacial adsorption behaviors

IFT change is a direct indication of liquid-liquid interfacial adsorption behaviors. Fig. 4(a) shows IFT changes under different conditions. The difference between DI water and brine can be ignored while the performances of nanoparticles were quite divergent.  $\text{SiO}_2$  decreased the IFT value by less than 10%, and the difference between initial and equilibrium stage was minor. However, GO and CNT-OH decreased the IFT value by 30–40% at the equilibrium stage. Although the absolute IFT reduction was not as dramatic as strong surfactants [10], a more significant dynamic change was observed. The dynamic effect originates from the slow accumulation at the liquid-liquid interface as a consequence of the longer diffusion time of nanoparticles compared to that of surfactant molecules [23,60]. The equilibrium time for nanoparticle adsorption is on the order of  $10^3$  to  $10^4$  s. In other words, particle

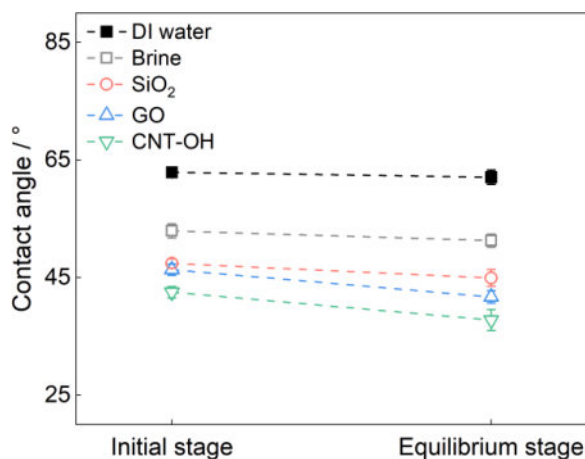


Fig. 3. Aqueous-phase contact angles of aqueous fluid/decane/quartz systems. The initial stage corresponds to the time that the interface formed. Significant wettability alternation was not observed in all cases, while the contact angle changes indicated nanoparticle adsorption capacities.

concentration at the interface is time-dependent. Considering the complex and irregular structure of porous media, the dynamic adsorption effects should be more pronounced in displacement processes.

The premise for Pickering emulsion stabilization is to hinder droplet coalescence by particle adsorption onto the interface. Fig. 4(c) presents the results of emulsification tests. For brine and  $\text{SiO}_2$  suspension, no emulsifying effect was observed after the mixing. The aqueous and oil phase remained separated with a clear interface. For GO and CNT-OH suspensions, significant emulsification occurred as indicated by the upper part of the mixture. Fig. 4(d) shows the inner structure of the emulsions after one week. The droplets were of ideal sphericity despite the polydispersity. Differences in emulsification and emulsion stabilization provide strong evidence for distinct interfacial adsorption properties. However, it should be noted that emulsification performances here rely on intense shear actions, which is hard to achieve during low-speed flow in porous media. Since no polar components in crude oil [61] or chemical additives [62] are involved in this study, the contribution of in-situ emulsification can be ignored for displacement processes.

We further analyzed the detachment energy to remove the particle from the liquid-liquid interface based on the free energy change. The detachment energy of an ideal spherical particle can be expressed as  $\Delta E = \pi r^2 \sigma (1 - \cos\theta)^2$  for transfer from the interface to the aqueous phase, where  $r$  is the particle radius,  $\sigma$  is the IFT, and  $\theta$  represents the surface wettability of particles [63,64]. For ideal sheet-like and fibrous materials, the expressions are found to be  $L^2 \sigma (1 - \cos\theta)$  and  $2rL\sigma(\sin\theta - \theta\cos\theta)$  respectively, where  $L$  is the characteristic length and  $r$  is the fiber diameter. Sheets and fibers possess much larger specific surface area than spheres, leading to higher detachment energy under similar conditions. Fig. 4(b) shows the estimated detachment energy for single particles. The relative differences are also valid for equal concentrations since the particle number densities are in the same order of magnitude (Table S.1 & Eq. (S.7)). For all  $\theta$ , sheets exhibit the highest  $\Delta E$  followed by fibers, which are both much larger than spheres. Such differences will be more significant considering their surface properties, as denoted by the points corresponding to the estimated surface wettability. For amphiphilic particles, the hydrophobic part tends to interact with the oil phase, while the hydrophilic sites prefer to remain in the aqueous phase. Higher  $\Delta E$  will facilitate the occurrence of irreversible adsorption events, as indicated by the characterization results. Details of the derivation and evaluation of the detachment energy are provided in the supplementary material.

IFT measurements, emulsification tests and particle detachment energy analysis elucidate differences in liquid-liquid interfacial adsorption behaviors. GO and CNT-OH yield stronger ability to reduce IFT and stabilize Pickering emulsions. Their sheet-like and fibrous shape corresponds to a much larger specific surface area and denser coverage compared to the spherical  $\text{SiO}_2$ . The amphiphilicity can further enhance the tendency to adsorb onto the liquid-liquid interface.

### 3.4. Solid surface adsorption behaviors

Solid surface adsorption is governed by intermolecular and surface forces when particles approaching the solid surface [65,66]. As shown in Fig. 5(a) and (b), all nanoparticles can spontaneously adsorb onto the solid surface, while the surface texture change varied significantly. The original surface was very smooth with a peak-to-valley roughness  $R_t$  of 10.2 nm and a root mean square roughness  $R_{\text{RMS}}$  of 1.5 nm. After  $\text{SiO}_2$  and CNT-OH treatment,  $R_t$  increased to 65.2 and 106.5 nm and  $R_{\text{RMS}}$  increased to 5.82 and 14.7 nm, respectively. The absolute roughness changes were not dramatic with peak-to-valley differences corresponding to maximum adsorption capacity of several layers of particles. The observations indicate uniformity of nanoparticle adsorption, which is consistent with some previous work [17,67]. Such adsorption states will not alter flow pathways or cause formation damage, while the coverage of nanoparticles changes the microscopic surface morphology. Fig. 5(c) compare the surface curvature distribution under different conditions.

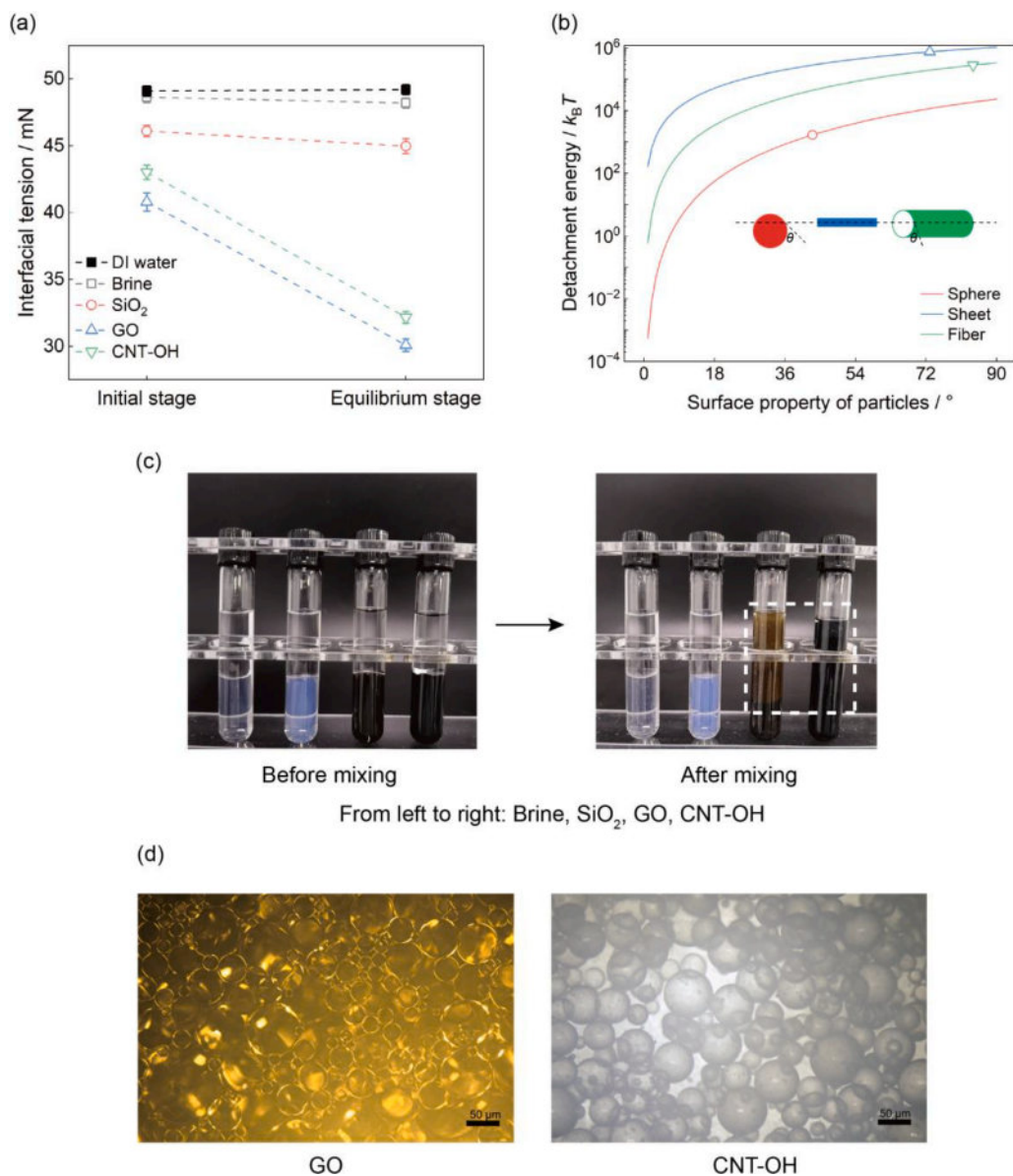


**Fig. 4.** Liquid-liquid interfacial adsorption characterizations and analysis. (a) Interfacial tensions of aqueous fluid/decane systems. The initial stage corresponds to the needle injection rate at 50  $\mu\text{L}/\text{min}$ . GO and CNT-OH decreased the IFT value up to 30–40% with a dynamic change from the initial to equilibrium stage. SiO<sub>2</sub> only influenced the IFT slightly. (b) Detachment energy versus surface wettability of spherical, sheet-like and fibrous nanoparticles based on different expressions. The parameters involved are from Table S.1,  $k_B$  is the Boltzmann constant and  $T$  is the absolute temperature. (c) Captured images before and after mixing. The volume ratio of the aqueous and oil phase is 1:1 in each tube. After mixing, the test-tubes were standing until phase separation was completed. Significant emulsification occurred when using GO and CNT-OH (denoted by the white dashed box), while brine and SiO<sub>2</sub> yielded no emulsifying effect. (d) Microscopic characterization of the inner structure of Pickering emulsions after one week.

Color change from blue to red corresponds to a continuous change in curvature from negative to positive. A dense network-like curvature distribution formed after SiO<sub>2</sub> adsorption and a similar wave-like structure was observed for the CNT-OH-treated substrate. Spheres are completely curved with a universal curvature in all directions. Fibers are only curved along the transverse direction. However, sheets with relatively flat surfaces are difficult to form effective curvature changes. In contrast to the performances of SiO<sub>2</sub> and CNT-OH, GO posed limited effect on surface topography. The presence of GO nanosheets on the solid surface can be identified by comparison with the original surface (Fig. 5(a) and (b)). The peak-to-valley roughness was even slightly lower after treatment ( $R_t = 6.2\text{nm}$ ) and the surface curvature variation was negligible compared to SiO<sub>2</sub> and CNT-OH.

The surface curvature distribution can highly impact microscopic wetting behaviors. In the three-phase contact region, the surface forces between interfaces should be incorporated into the augmented Young-Laplace equation,  $P_C = \sigma\kappa + \Pi(h)$ , where  $P_C$  is the capillary pressure,  $\kappa$  is the interfacial curvature and  $\Pi(h)$  is the disjoining pressure only significant in the thin-film region. Considering the quasi-equilibrium state under given  $P_C$ , the surface morphology determines the interfacial curvature and thereby the water film distribution. For concave

valleys,  $\kappa > 0$  and the water film tends to accumulate and thicken. For convex tips,  $\kappa < 0$  and  $P_C$  has to be balanced by  $\Pi(h)$ . The water film tends to be thinner to keep the force balance [68]. When  $P_C > \sigma\kappa + \Pi_c$ , where  $\Pi_c$  is the critical disjoining pressure, the film will rupture and the solid surface will be covered by the oil phase. Therefore, connected valleys are the premise for water film spreading and stabilization, which may enhance the detachment of the trapped oil phase.

We further investigated the influence of nanoparticle adsorption on the wetting film state by film transition modeling. The augmented Young-Laplace equation was numerically solved and the film configuration on the surfaces under equilibrium state was obtained, as shown in Fig. 5(d). It is found that connected and stable water films can only develop on the rough structures after SiO<sub>2</sub> and CNT-OH treatments owing to the formation of connected valleys. Fig. 5(e) presents the disjoining pressure isotherms considering different surface properties after nanoparticle adsorption. The typical trend of disjoining pressure versus film thickness is non-monotonic, reaching  $\Pi_c$  at a few nanometers. The similarity between the curves indicates that surface morphology should be a more dominant factor. The average film thickness and surface coverage of SiO<sub>2</sub>-treated and CNT-OH-treated cases are much larger than those of untreated and GO-treated, as shown in Fig. 5(f). Details of

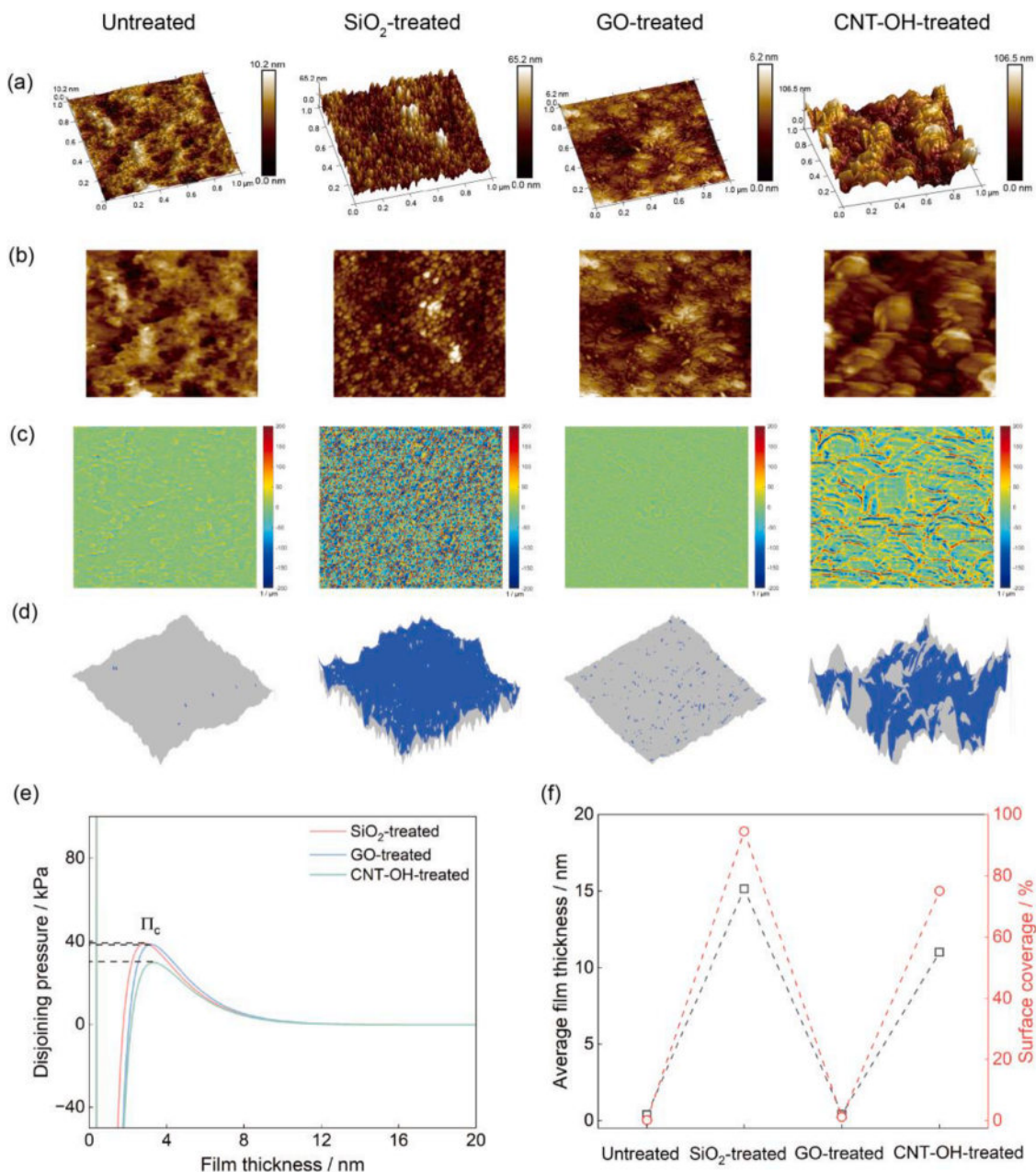


**Fig. 5.** Solid surface adsorption characterizations and analysis. (a) AFM images of the 3D surface topography. SiO<sub>2</sub> and CNT-OH changed the morphology significantly while GO slightly smoothed the surface. (b) AFM images of the 2D deflection signals. The presence of nanoparticles with different shapes on the surfaces can be observed clearly. (c) Surface curvature distribution calculated based on height information. The surfaces treated by SiO<sub>2</sub> and CNT-OH exhibited network-like and wave-like curvature changes respectively, while GO adsorption induced negligible change. (d) Water film distribution modelled by solving the augmented Young-Laplace equation. The blue parts are covered by robust water films while the gray parts correspond to the rupture of films. Surface roughness formed by spherical SiO<sub>2</sub> and fibrous CNT-OH is beneficial to the formation and maintenance of water films. (e) Disjoining pressure isotherms.  $\Pi_c$  is the critical disjoining pressure determining film stabilization or rupture. (f) Statistics of the average film thickness and coverage. The film can only develop after SiO<sub>2</sub> and CNT-OH treatments, where SiO<sub>2</sub> performs the best.

the surface curvature distribution calculation, expressions and parameters for the disjoining pressure, and the water film distribution modeling are provided in the supplementary material.

Surface topography characterization, curvature distribution analysis and film transition modeling illustrate differences in solid surface adsorption behaviors. SiO<sub>2</sub> and CNT-OH yield stronger ability to form nanoscale rough structures and stabilize water films. Their spherical and fibrous curved surfaces can induce continuous curvature change, which corresponds to the formation of connected valleys. GO nanosheets can also adsorb onto the solid surface but with minor impact on the surface texture. The hydrophilicity of SiO<sub>2</sub> can further enhance film spreading,

which will be verified by the displacement experiments.

### 3.5. Enhanced displacement performance: phase distribution and time evolution

A series of displacement experiments were performed on the Matrix structure with thermally oxidized water-wet surface. As shown in Fig. 6, the final phase distributions differed greatly using different invading fluids. For brine, the displacement efficiency was the lowest with fingering pathways. All nanoparticle suspensions can enhance displacement performance significantly but to varying degrees. CNT-OH

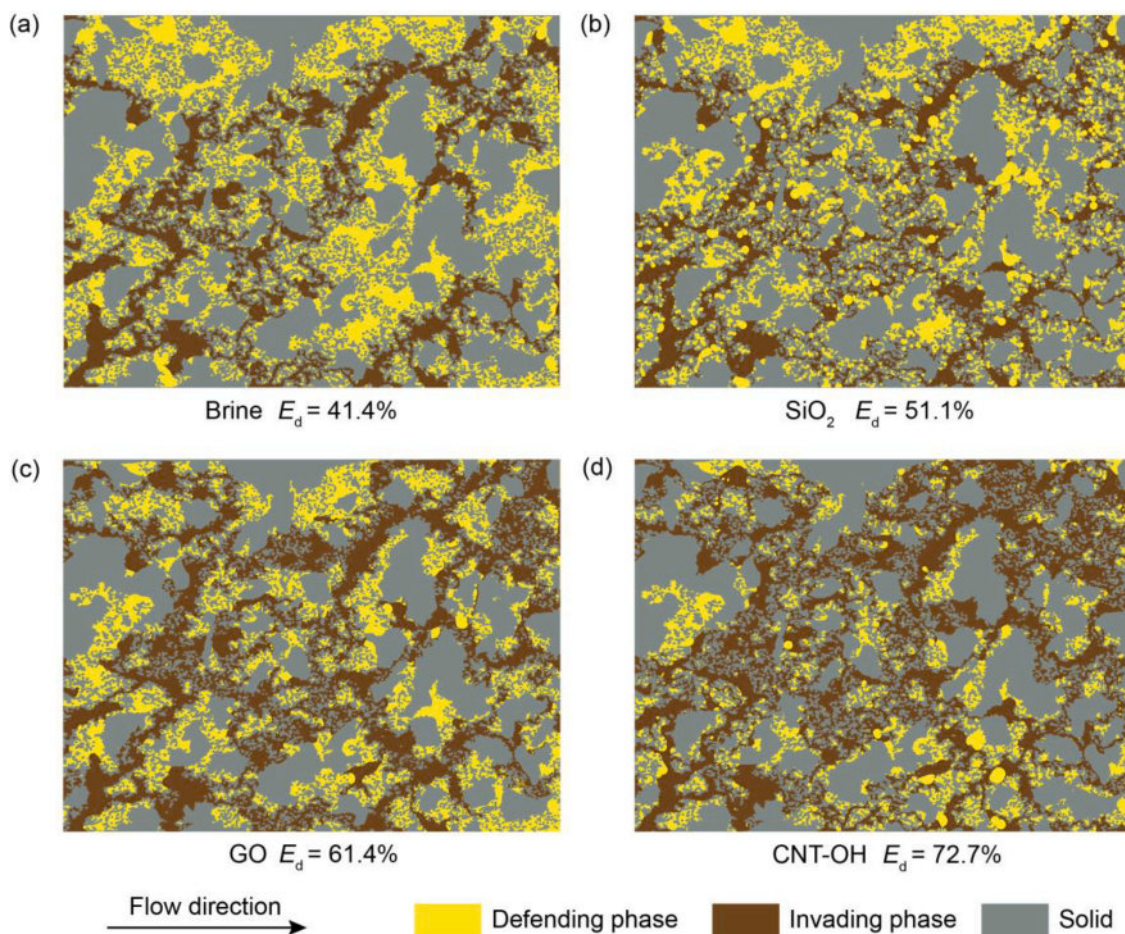


**Fig. 6.** Final phase distributions when injecting (a) brine, (b)  $\text{SiO}_2$  suspension, (c) GO suspension, and (d) CNT-OH suspension. All nanoparticles can enhance displacement performance but to different degrees with different flow patterns.

yielded the optimal performance with a maximum displacement efficiency of up to 72.7%, followed by GO and then  $\text{SiO}_2$ . The displacement patterns also show clear distinction.  $\text{SiO}_2$  promoted the peeling and detachment of oil blobs in swept regions, manifested as the discrete state of the defending phase. However, large clusters in un-swept regions were less influenced. GO promoted invasion into un-swept regions, creating thicker and longer invading path. Meanwhile, no similar pattern as  $\text{SiO}_2$  was observed. CNT-OH exhibited a mixed feature of GO and  $\text{SiO}_2$ , which corresponds to optimal performance. We further quantified the phase saturation evolution in the displacement processes. It is interesting to find that the relative performances varied in different stages. As shown in Fig. 7(a),  $\text{SiO}_2$  performed better during the earlier period with a much slower breakthrough and higher recovery. Nevertheless, phase saturation varied little after that (Fig. 7(b)). In contrast, GO showed relatively weaker ability to influence the displacement pattern initially, but achieved stepped recovery over a long period. CNT-OH induced continuous recovery with advantages of both. Fig. 7(c) and (d) show the displacement efficiency variation. At the breakthrough stage,  $\text{SiO}_2$  exhibited a slightly higher displacement efficiency than CNT-OH and GO. At the final stage, CNT-OH achieved the highest efficiency and GO overtook  $\text{SiO}_2$ .

### 3.6. Typical displacement enhancement modes

Behind the difference in displacement performances is the difference in displacement patterns. We captured and clarified two typical displacement enhancement modes based on pore-scale observations, which are related to different adsorption behaviors.

As shown in Fig. 8, during GO and CNT-OH suspension flooding, the invading phase entered the un-swept regions randomly and frequently at the post-breakthrough stage over a long period. Residual oil can be effectively mobilized and sweeping efficiency was significantly enhanced. The invasion into un-swept regions manifests as localized interfacial instability, i.e., the invading phase entered from one interface along the flow direction with the lowest resistance, and displaced the defending phase occupying the pore space out from another interface. The process of a single invasion was rapid with a piston-type feature. This phenomenon was hardly observed when using  $\text{SiO}_2$ , which is consistent with differences in liquid-liquid adsorption behaviors.

Considering a residual ganglion in contact with the invading phase through multiple interfaces around the un-swept porous region. When breakthrough occurs, the capillary and viscous forces exerted on the entire ganglion are close to equilibrium, leading to its trapping. The only way to mobilize the ganglion is to break the equilibrium state and create a larger driven force than the resistant force. The viscous pressure drop across a ganglion is given by Darcy's law,  $\Delta P_v = \mu UL/K$ , where  $\mu$  is the invading phase viscosity,  $U$  is the characteristic velocity,  $L$  is the ganglion length, and  $K$  is the modified permeability considering the existence of trapped oil [58]. The capillary force exerted on a ganglion is the summation of Laplace pressure,  $\Delta P_c = \sum_i \sigma_i \cos \theta_i / R_i$ , where  $\sigma_i$ ,  $\theta_i$ ,  $R_i$  are the IFT, apparent contact angle and mean interfacial curvature of interface  $i$  respectively. Under the given low capillary number condition, interfacial parameter change induced by nanoparticle adsorption should be the most possible mechanism. As presented in Section 3.3, the dynamic IFT effect of GO and CNT-OH is significant compared to  $\text{SiO}_2$ . The stronger ability of GO and CNT-OH to adsorb onto the interface can

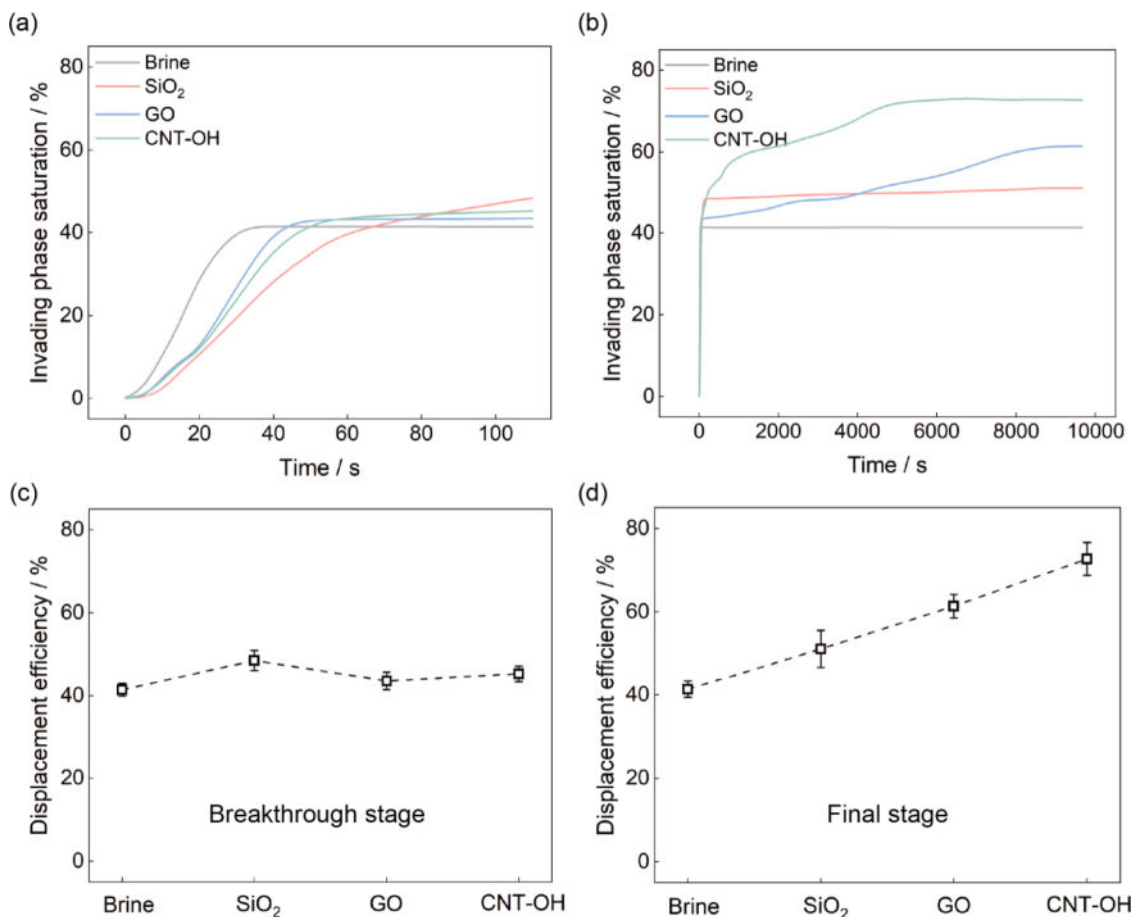


**Fig. 7.** Time evolution of phase saturation and comparison of displacement efficiency at different stages. (a) shows the breakthrough process, corresponding to the rapidly rising part on the left of the curves in (b). SiO<sub>2</sub> performed better during the earlier period with a much slower breakthrough and higher recovery. GO performed better after that with stepped recovery over a long period. CNT-OH exhibited a mixed feature of both with optimal performance. (c) Displacement efficiency at the breakthrough stage. SiO<sub>2</sub> performed the best, followed by CNT-OH and then GO. (d) Displacement efficiency at the final stage. CNT-OH performed the best and GO overtook SiO<sub>2</sub>.

induce IFT change with time. In porous media, the irregular structure and complex flow field distribution will lead to non-uniform concentration distribution naturally [69]. The coupling of dynamic adsorption and velocity variation can change the capillary force gradually and locally, which explains the occurrence of oil mobilization long after breakthrough. When the accumulation reaches a critical state, the balance will be broken and the phase distribution will be changed. The mobilization of one oil cluster can strengthen fluctuations, which may accelerate the processes. Optical images captured immediately after the displacement experiments also verified our analysis, as shown on the right side of Fig. 8. It is worth mentioning that the fluorescence decay in the oil phase was found to be more inhomogeneous during experiments when using GO and CNT-OH, where the fluorescence intensity decayed faster near the interface. Although this had little impact on binarization, it should suggest stronger interfacial interactions.

Fig. 9 presents another typical mode. During SiO<sub>2</sub> and CNT-OH suspension flooding, the trapped oil in the swept region was broken and detached in the form of isolated ganglia. The invading phase spread into the dead-end or dead-end-like structures spontaneously and deposited at the valleys. The development of deposited films and the capillary pressure difference between the outer and inner interfaces drove the removal of the residual oil, which can then be transported through the main channels. Different from the piston-type invasion into the un-swept region, the detachment of isolated ganglia was a relatively slow process lasting for approximately 100 to 300 s. Moreover, the efficient displacement was only significant near the breakthrough stage,

especially for SiO<sub>2</sub>. Breakthrough will also be delayed as the invading phase entered more dense and tortuous pores, as shown in Fig. 7(a). This phenomenon was hardly observed when using GO, which is consistent with differences in solid surface adsorption behaviors.

In Section 3.4, we analyzed the relationship between solid surface adsorption and wetting film transition. SiO<sub>2</sub> and CNT-OH yield stronger ability to form nanoscale rough structures with continuous curvature change, which is beneficial for the formation and stabilization of water films. In porous media, the original surface is more irregular and non-smooth. The hierarchical micro-nano structure can further promote the development of wetting films and the removal of residual oil. On the one hand, surface adsorption and film accumulation are synchronous, so the characteristic time for oil detachment is relatively longer. On the other hand, after the films are fully developed in swept regions, driven force for residual oil mobilization is lacking, so displacement enhancement was only significant near the breakthrough stage.

### 3.7. Topological analysis: ganglia number and volume fraction of larger clusters

Statistics of phase distribution topology provide fundamental information on multiphase displacement consequences. Each ganglion of the defending phase can be recognized by image processing techniques. To verify and quantify the displacement enhancement modes, we investigated the evolution of the volume fraction of larger clusters  $V_l$  and oil ganglion number  $N_g$ .

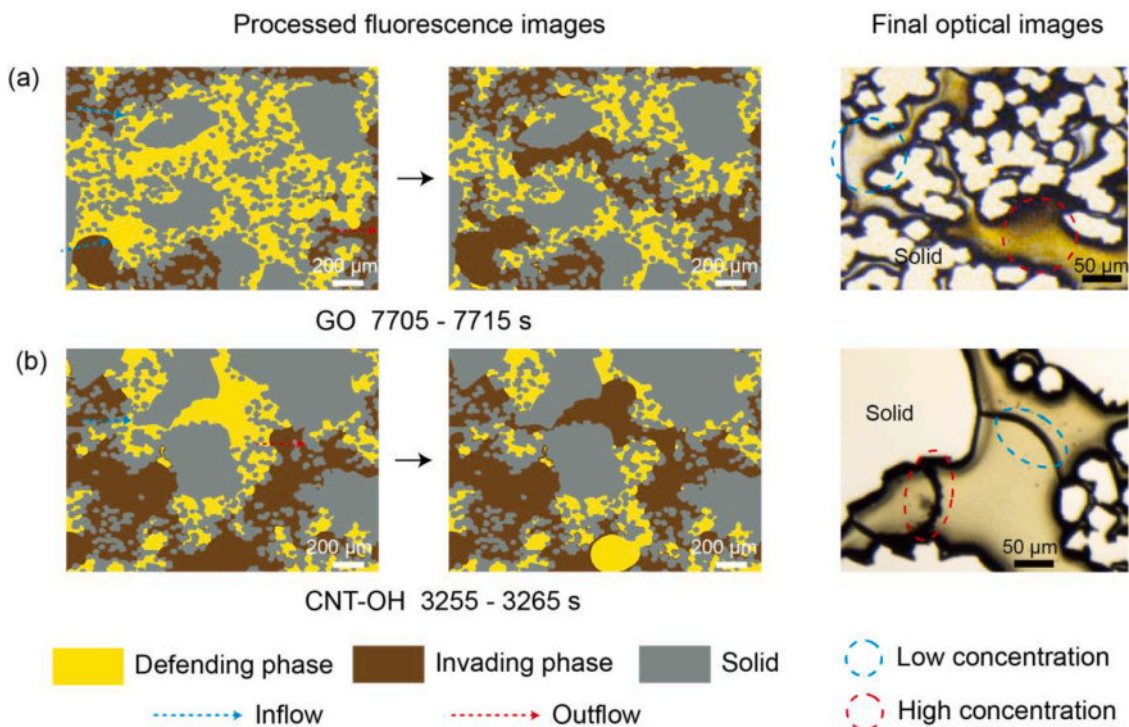


**Fig. 8.** Displacement enhancement mode 1: localized interfacial instability and sweeping efficiency enhancement. At the post-breakthrough stage, piston-type invasion into un-swept regions occurred randomly and frequently. (a) and (b) are two typical cases of this phenomenon, which was mainly observed during GO and CNT-OH suspension flooding. A single invasion event usually completed in a very short time (less than 10 s). Optical images captured under coaxial epi-illumination at the final stage reflected the non-uniform concentration distribution of nanoparticles with a tendency to accumulate near the interface.

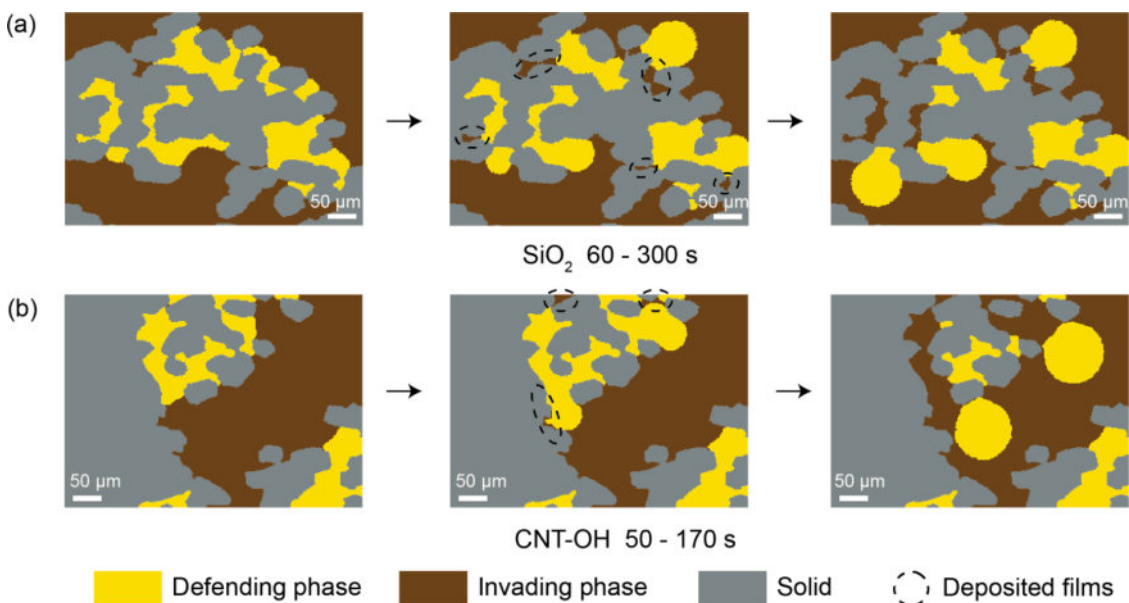


**Fig. 9.** Displacement enhancement mode 2: film spreading and oil ganglion detachment. Near the breakthrough stage, film deposition in dead-end or dead-end-like structures was widely observed and the residual oil can be broken and detached. (a) and (b) are two typical cases of this phenomenon, which was mainly observed during SiO<sub>2</sub> and CNT-OH suspension flooding. The development usually lasted for approximately 100–300 s, which corresponds to the solid surface adsorption and film deposition process.

As shown in Fig. 10(a) and (c), lower volume fractions of larger clusters were reached in the presence of CNT-OH and GO, while SiO<sub>2</sub> exhibited a weaker effect. Reduction in  $V_1$  mainly reflects invasion into un-swept regions, which corresponds to differences in mode 1 and thereby in liquid-liquid interfacial adsorption. Meanwhile, it is found that  $V_1$  of SiO<sub>2</sub> suspension flooding at the breakthrough stage was lower

than that of GO, which can be explained by the higher displacement efficiency in swept regions owing to mode 2. The changes of  $V_1$  from breakthrough stage to final stage were dramatic for GO and CNT-OH, while for SiO<sub>2</sub> it remained stable after breakthrough.

As presented in Fig. 10(b) and (d), more ganglia were formed in the existence of SiO<sub>2</sub>, followed by CNT-OH. However, the ganglion number

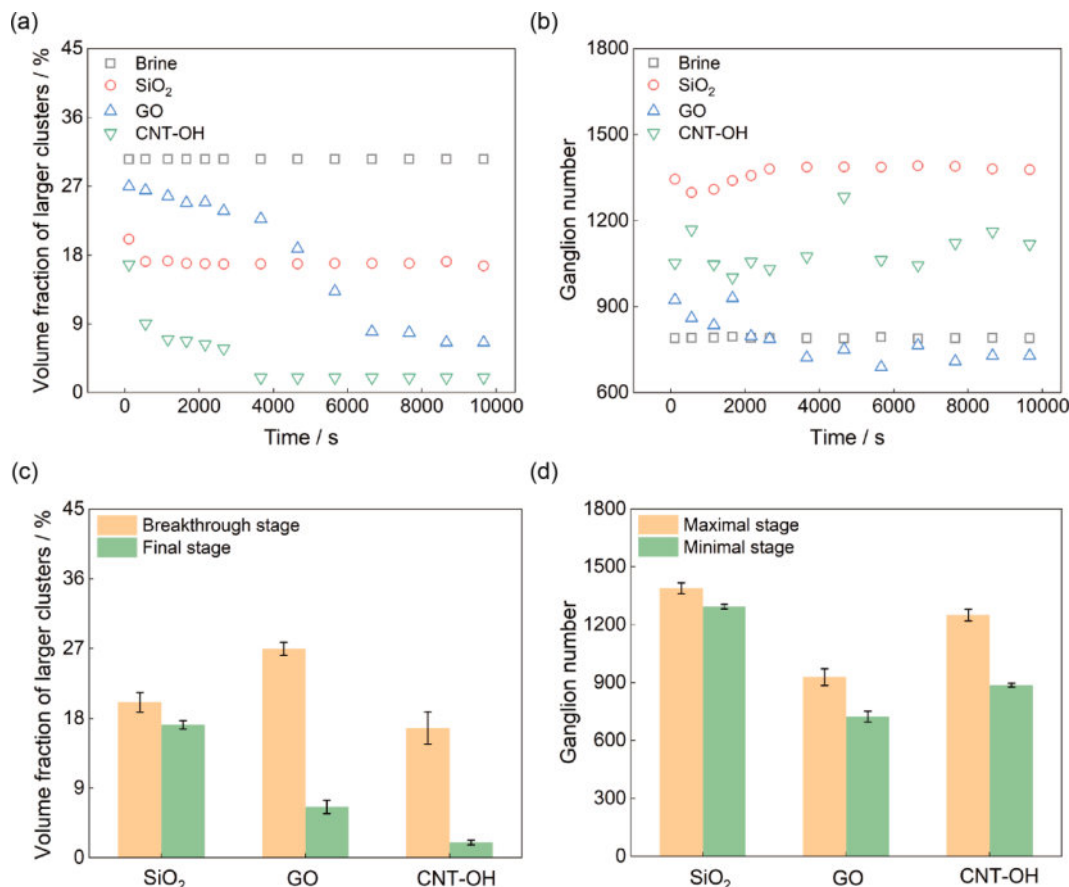


**Fig. 10.** Topological analysis. (a) and (b) show the evolution of the volume fraction of larger clusters  $V_1$  and oil ganglion number  $N_g$  versus time after breakthrough, respectively. (c)  $V_1$  at the breakthrough and final stage. (d)  $N_g$  at the maximal and minimal values. GO and CNT-OH reduced  $V_1$  more significantly by mode 1, while SiO<sub>2</sub> and CNT-OH increased  $N_g$  to higher values by mode 2, both consistent with differences in adsorption behaviors. Moreover, SiO<sub>2</sub> suspension flooding exhibited lower  $V_1$  at the breakthrough stage than that of GO, while  $N_g$  fluctuated more when using GO and CNT-OH.

when using GO suspension fell in the same range as when using brine. Increase in  $N_g$  mainly reflects formation and detachment of oil blobs, which corresponds to differences in mode 2 and thereby in solid surface adsorption. Besides, the fluctuations in  $N_g$  of CNT and GO were more pronounced than SiO<sub>2</sub>, which indicates stronger ability in residual oil transport related to mode 1. The discrete oil droplets can be more difficult to displace due to the uniformity of the interface [70].

### 3.8. Discussions: substrate property and heterogeneity of the porous media

The properties of the porous media may impact displacement performance evaluation. We also performed experiments on PFP structures with similar water-wet surface and Matrix structures with oil-wet silane-modified surface. Fig. 11 shows the final displacement efficiency enhancements in different porous media. In the first place, the relative performances are consistent in all cases, i.e., CNT-OH achieved the highest enhancement, followed by GO and then SiO<sub>2</sub>. Interestingly, the performance variations with substrate property and structure heterogeneity were different. For Matrix structures with more hydrophobic surface, the displacement performances of SiO<sub>2</sub> and CNT-OH were weakened while that of GO was barely affected. The oil-wet state of solid surface can undermine wetting film spreading driven by solid surface adsorption behaviors, which was important for SiO<sub>2</sub> and CNT-OH but played minor role in the displacement enhancement by GO. For PFP structures with similar substrate property, the displacement performances were all weakened. Under dominated preferential flow, the lower interfacial contact area and weaker local interactions suppressed the adsorption effects and corresponding displacement enhancement

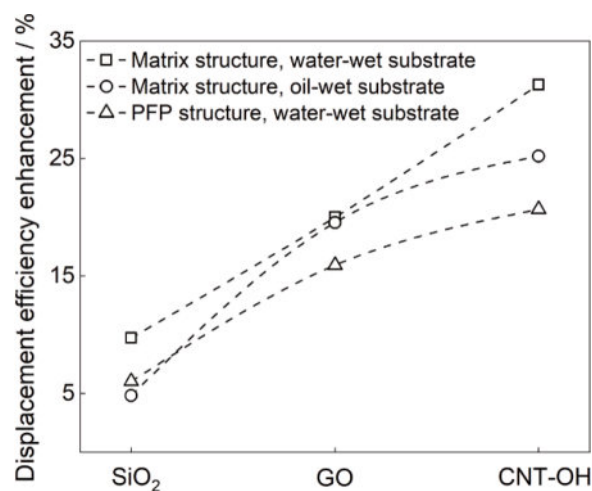


**Fig. 11.** Displacement efficiency enhancement on different structures and substrates. The relative performances are consistent in all cases. Dominated preferential flow will weaken displacement enhancements of all nanoparticles similarly, while oil-wet state of the substrate mainly suppresses wetting state transition and therefore the performances of SiO<sub>2</sub> and CNT-OH.

modes.

#### 4. Conclusions

In this study, three kinds of representative nanoparticles with promising industrial applications and unique material properties were systematically compared based on experimental observations and mechanism analysis. The selected nanoparticles yield clear distinctions in adsorption behaviors and displacement patterns. GO performs better in liquid-liquid interfacial adsorption, which promotes sweeping efficiency enhancement via localized invasion into un-swept regions. SiO<sub>2</sub> performs better in solid surface adsorption, which promotes residual oil detachment via film development in swept regions. CNT-OH exhibits the optimal performance with synergistic effects of both modes. Changes in substrate property and structure heterogeneity will weaken their performances in different aspects.

Differences in adsorption behaviors and displacement patterns are highly consistent, which are determined by particle shapes and surface properties. Spherical and fibrous particles with curved surfaces can effectively form structured solid surfaces, while sheet-like and fibrous particles with large specific surface areas tend to retain at the liquid-liquid interface. Hydrophilicity will further promote film spreading, whereas amphiphilicity can increase detachment energy.

Moving forward, more factors require consideration for engineering applications, which include but are not limited to harsh conditions in the underground, complexity of the defending fluid, optimal size and concentration condition, and surface modifications. Regardless, our results clarify particle shape and surface property effects on the design and application of nanomaterials for displacement enhancement.

#### CRedit authorship contribution statement

**Xukang Lu:** Investigation, Software, Validation, Investigation, Writing – original draft. **Moran Wang:** Conceptualization, Supervision, Writing – review & editing, Project administration.

#### Declaration of Competing Interest

The authors declare that they have no known competing financial interests or personal relationships that could have appeared to influence the work reported in this paper.

#### Data availability

No data was used for the research described in the article.

#### Acknowledgments

This work is financially supported by the National Key Research and Development Program of China (No. 2019YFA0708704) and the NSF grant of China (No. 12272207, U1837602).

#### Supplementary materials

Supplementary material associated with this article can be found, in the online version, at [doi:10.1016/j.ijmecsci.2023.108471](https://doi.org/10.1016/j.ijmecsci.2023.108471).

#### References

- Lei W, Lu X, Wang M. Multiphase displacement manipulated by micro/nanoparticle suspensions in porous media via microfluidic experiments: from interface science to multiphase flow patterns. *Adv Colloid Interface Sci* 2023;311:102826.
- Huppert HE, Neufeld JA. The fluid mechanics of carbon dioxide sequestration. *Annu Rev Fluid Mech* 2014;46(1):255–72.
- Pak T, LFDL L, Tosco T, Costa GSR, Rosa PRR, Archilha NL. Pore-scale investigation of the use of reactive nanoparticles for in situ remediation of contaminated groundwater source. *Proc Natl Acad Sci USA* 2020;117(24):13366–73.
- Sackmann EK, Fulton AL, Beebe DJ. The present and future role of microfluidics in biomedical research. *Nature* 2014;507(7491):181–9.
- Xie C, Lei W, Balhoff MT, Wang M, Chen S. Self-adaptive preferential flow control using displacing fluid with dispersed polymers in heterogeneous porous media. *J Fluid Mech* 2021;906:A10.
- Liu F, Wang M. Review of low salinity waterflooding mechanisms: wettability alteration and its impact on oil recovery. *Fuel* 2020;267:117112.
- Liu F, Wang M. Wettability effects on mobilization of ganglia during displacement. *Int J Mech Sci* 2021;215:106933.
- Lei W, Li Q, Yang H-E, Wu T-J, Wei J, Wang M. Preferential flow control in heterogeneous porous media by concentration-manipulated rheology of microgel particle suspension. *J Pet Sci Eng* 2022;212:110275.
- Lei W, Lu X, Wu T, Yang H, Wang M. High-performance displacement by microgel-in-oil suspension in heterogeneous porous media: microscale visualization and quantification. *J Colloid Interface Sci* 2022;627:848–61.
- Yang W, Lu J, Wei B, Yu H, Liang T. Micromodel studies of surfactant flooding for enhanced oil recovery: a review. *ACS Omega* 2021;6(9):6064–9.
- Sun X, Zhang Y, Chen G, Gai Z. Application of nanoparticles in enhanced oil recovery: a critical review of recent progress. *Energies* 2017;10(3):345.
- Foroozesh J, Kumar S. Nanoparticles behaviors in porous media: application to enhanced oil recovery. *J Mol Liq* 2020;316:113876.
- Peng B, Zhang L, Luo J, Wang P, Ding B, Zeng M, et al. A review of nanomaterials for nanofluid enhanced oil recovery. *RSC Adv* 2017;7(51):32246–54.
- Jiang Y, Zhou X. Analysis of flow and heat transfer characteristics of nanofluids surface tension driven convection in a rectangular cavity. *Int J Mech Sci* 2019;153:154–63.
- Mondal MK, Biswas N, Datta A, Sarkar BK, Manna NK. Positional impacts of partial wall translations on hybrid nanofluid flow in porous media: real Coded Genetic Algorithm (RCGA). *Int J Mech Sci* 2022;217:107030.
- Kashyap D, Dass AK. Effect of boundary conditions on heat transfer and entropy generation during two-phase mixed convection hybrid Al<sub>2</sub>O<sub>3</sub>-Cu/water nanofluid flow in a cavity. *Int J Mech Sci* 2019;157–158:45–59.
- Dehghan Monfared A, Ghazanfari MH, Jamialahmadi M, Helalizadeh A. Adsorption of silica nanoparticles onto calcite: equilibrium, kinetic, thermodynamic and DLVO analysis. *Chem Eng J* 2015;281:334–44.
- Al-Ansari S, Barifcani A, Wang S, Maxim L, Iglauer S. Wettability alteration of oil-wet carbonate by silica nanofluid. *J Colloid Interface Sci* 2016;461:435–42.
- Giraldo J, Benjumea P, Lopera S, Cortés FB, Ruiz MA. Wettability alteration of sandstone cores by alumina-based nanofluids. *Energy Fuels* 2013;27(7):3659–65.
- Khoramian R, Ramazani SA A, Hekmatzadeh M, Kharat R, Asadian E. Graphene oxide nanosheets for oil recovery. *ACS Appl Nano Mater* 2019;2(9):5730–42.
- Ghalamizade Elyaderani SM, Jafari A, Razavinezhad J. Experimental investigation of mechanisms in functionalized multiwalled carbon nanotube flooding for enhancing the recovery from heavy-oil reservoirs. *SPE J* 2019;24(06):2681–94.
- Li S, Hadia NJ, Lau HC, Torsæter O, Stubbs LP, Ng QH. Silica nanoparticles suspension for enhanced oil recovery: stability behavior and flow visualization. In: *Proceedings of the SPE Europec featured at 80th EAGE conference and exhibition*; 2018.
- Xu K, Zhu P, Huh C, Balhoff MT. Microfluidic investigation of nanoparticles' role in mobilizing trapped oil droplets in porous media. *Langmuir* 2015;31(51):13673–9.
- Tajik S, Shahrabadi A, Rashidi A, Jalilian M, Yadegari A. Application of functionalized silica-graphene nanohybrid for the enhanced oil recovery performance. *Colloids Surf A: Physicochem Eng Asp* 2018;556:253–65.
- Radnia H, Rashidi A, Solaimany Nazar AR, Eskandari MM, Jalilian M. A novel nanofluid based on sulfonated graphene for enhanced oil recovery. *J Mol Liq* 2018;271:795–806.
- Yoon KY, An SJ, Chen Y, Lee JH, Bryant SL, Ruoff RS, et al. Graphene oxide nanoplatelet dispersions in concentrated NaCl and stabilization of oil/water emulsions. *J Colloid Interface Sci* 2013;403:1–6.
- Nikolov A, Wu P, Wasan D. Structure and stability of nanofluid films wetting solids: an overview. *Adv Colloid Interface Sci* 2019;264:1–10.
- Lim S, Zhang H, Wu P, Nikolov A, Wasan D. The dynamic spreading of nanofluids on solid surfaces – role of the nanofilm structural disjoining pressure. *J Colloid Interface Sci* 2016;470:22–30.
- Zhang H, Nikolov A, Wasan D. Enhanced oil recovery (EOR) using nanoparticle dispersions: underlying mechanism and imbibition experiments. *Energy Fuels* 2014;28(5):3002–9.
- Zhang H, Ramakrishnan TS, Nikolov A, Wasan D. Enhanced oil recovery driven by nanofilm structural disjoining pressure: flooding experiments and microvisualization. *Energy Fuels* 2016;30(4):2771–9.
- Hu Z, Azmi SM, Raza G, Glover PWJ, Wen D. Nanoparticle-assisted water-flooding in Berea sandstones. *Energy Fuels* 2016;30(4):2791–804.
- Arani AAA, Sadripour S, Kermani S. Nanoparticle shape effects on thermal-hydraulic performance of boehmite alumina nanofluids in a sinusoidal-wavy mini-channel with phase shift and variable wavelength. *Int J Mech Sci* 2017;128–129:550–63.
- Shahsavari A, Farhadi P, Yildiz C, Moradi M, Arici M. Evaluation of entropy generation characteristics of boehmite-alumina nanofluid with different shapes of nanoparticles in a helical heat sink. *Int J Mech Sci* 2022;225:107338.
- Shahsavari A, Moradi K, Yildiz C, Farhadi P, Arici M. Effect of nanoparticle shape on cooling performance of boehmite-alumina nanofluid in a helical heat sink for laminar and turbulent flow regimes. *Int J Mech Sci* 2022;217:107045.

- [35] Gao H-M, Lu Z-Y, Liu H, Sun Z-Y, An L-J. Orientation and surface activity of Janus particles at fluid-fluid interfaces. *J Chem Phys* 2014;141(13):134907.
- [36] Cao J, Chen Y, Xu G, Wang X, Li Y, Zhao S, et al. Study on interface regulation effects of Janus nanofluid for enhanced oil recovery. *Colloids Surf A: Physicochem Eng Asp* 2022;653:129880.
- [37] Xie D, Jiang Y, Li K, Yang X, Zhang Y. Pickering emulsions stabilized by mesoporous nanoparticles with different morphologies in combination with DTAB. *ACS Omega* 2022;7(33):29153–60.
- [38] Luo D, Wang F, Zhu J, Cao F, Liu Y, Li X, et al. Nanofluid of graphene-based amphiphilic Janus nanosheets for tertiary or enhanced oil recovery: high performance at low concentration. *Proc Natl Acad Sci USA* 2016;113(28):7711–6.
- [39] Alzobaidi S, Wu P, Da C, Zhang X, Hackbarth J, Angeles T, et al. Effect of surface chemistry of silica nanoparticles on contact angle of oil on calcite surfaces in concentrated brine with divalent ions. *J Colloid Interface Sci* 2021;581:656–68.
- [40] Hatchell D, Song W, Daigle H. Effect of interparticle forces on the stability and droplet diameter of Pickering emulsions stabilized by PEG-coated silica nanoparticles. *J Colloid Interface Sci* 2022;626:824–35.
- [41] Sun N, Yao X, Xu Z, Li J, Yang N, Lyu D, et al. Janus nanographene oxide with aerophilic/hydrophilic characteristics for enhancing foam stability in high-temperature reservoirs. *J Mol Liq* 2023;371:121087.
- [42] Nazari Moghaddam R, Bahramian A, Fakhroei Z, Karimi A, Arya S. Comparative study of using nanoparticles for enhanced oil recovery: wettability alteration of carbonate rocks. *Energy Fuels* 2015;29(4):2111–9.
- [43] Alomair OA, Matar KM, Alsaeed YH. Experimental study of enhanced-heavy-oil recovery in Berea sandstone cores by use of nanofluids applications. *SPE Reserv Eval Eng* 2015;18(03):387–99.
- [44] Nwidae LN, Al-Anssari S, Barifcani A, Sarmadivaleh M, Lebedev M, Iglauer S. Nanoparticles influence on wetting behaviour of fractured limestone formation. *J Pet Sci Eng* 2017;149:782–8.
- [45] Ju B, Fan T. Experimental study and mathematical model of nanoparticle transport in porous media. *Powder Technol* 2009;192(2):195–202.
- [46] Anbari A, Chien H-T, Datta SS, Deng W, Weitz DA, Fan J. Microfluidic model porous media: fabrication and applications. *Small* 2018;14(18):1703575.
- [47] Gerami A, Alzahid Y, Mostaghimi P, Kashaninejad N, Kazemifar F, Amirian T, et al. Microfluidics for porous systems: fabrication, microscopy and applications. *Transp Porous Media* 2019;130(1):277–304.
- [48] Kumar Gunda NS, Bera B, Karadimitriou NK, Mitra SK, Hassanizadeh SM. Reservoir-on-a-Chip (ROC): a new paradigm in reservoir engineering. *Lab Chip* 2011;11(22):3785–92.
- [49] Lei W, Liu T, Xie C, Yang H, Wu T, Wang M. Enhanced oil recovery mechanism and recovery performance of micro-gel particle suspensions by microfluidic experiments. *Energy Sci Eng* 2020;8(4):986–98.
- [50] Stanley CE, Grossmann G, Casadevall i Solvas X, deMello AJ. Soil-on-a-Chip: microfluidic platforms for environmental organismal studies. *Lab Chip* 2016;16(2):228–41.
- [51] Mejia L, Zhu P, Hyman JD, Mohanty KK, Balhoff MT. Coreflood on a chip: core-scale micromodels for subsurface applications. *Fuel* 2020;281:118716.
- [52] Marciano DC, Kosynkin DV, Berlin JM, Sinitiskii A, Sun Z, Slesarev A, et al. Improved synthesis of graphene oxide. *ACS Nano* 2010;4(8):4806–14.
- [53] Kim J, Cote LJ, Kim F, Yuan W, Shull KR, Huang J. Graphene oxide sheets at interfaces. *J Am Chem Soc* 2010;132(23):8180–6.
- [54] Osorio AG, Silveira ICL, Bueno VL, Bergmann CP. H<sub>2</sub>SO<sub>4</sub>/HNO<sub>3</sub>/HCl—Functionalization and its effect on dispersion of carbon nanotubes in aqueous media. *Appl Surf Sci* 2008;255(5):2485–9.
- [55] Sotirelis NP, Chrysikopoulos CV. Interaction between graphene oxide nanoparticles and quartz sand. *Environ Sci Technol* 2015;49(22):13413–21.
- [56] Chomsurin C, Werth CJ. Analysis of pore-scale nonaqueous phase liquid dissolution in etched silicon pore networks. *Water Resour Res* 2003;39(9):1265.
- [57] Lei W, Lu X, Liu F, Wang M. Non-monotonic wettability effects on displacement in heterogeneous porous media. *J Fluid Mech* 2022;942:R5.
- [58] Datta SS, Ramakrishnan TS, Weitz DA. Mobilization of a trapped non-wetting fluid from a three-dimensional porous medium. *Phys Fluids* 2014;26(2):022002.
- [59] Lenormand R, Touboul E, Zarcone C. Numerical models and experiments on immiscible displacements in porous media. *J Fluid Mech* 1988;189:165–87.
- [60] Rana S, Yu X, Patra D, Moyano DF, Miranda OR, Hussain I, et al. Control of surface tension at liquid–liquid interfaces using nanoparticles and nanoparticle–protein complexes. *Langmuir* 2012;28(4):2023–7.
- [61] Xu K, Agrawal D, Darugar Q. Hydrophilic nanoparticle-based enhanced oil recovery: microfluidic investigations on mechanisms. *Energy Fuels* 2018;32(11):11243–52.
- [62] Du Y, Xu K, Mejia L, Balhoff M. Surface-active compounds induce time-dependent and non-monotonic fluid-fluid displacement during low-salinity water flooding. *J Colloid Interface Sci* 2023;631:245–59.
- [63] Creighton MA, Ohata Y, Miyawaki J, Bose A, Hurt RH. Two-dimensional materials as emulsion stabilizers: interfacial thermodynamics and molecular barrier properties. *Langmuir* 2014;30(13):3687–96.
- [64] Sarkar A, Dickinson E. Sustainable food-grade Pickering emulsions stabilized by plant-based particles. *Curr Opin Colloid Interface Sci* 2020;49:69–81.
- [65] Israelachvili JN. Intermolecular and surface forces. 3rd ed. Cambridge, MA: Academic Press; 2011.
- [66] Ramezanzpour M, Siavashi M, Raeini AQ, Blunt MJ. Pore-scale simulation of nanoparticle transport and deposition in a microchannel using a Lagrangian approach. *J Mol Liq* 2022;355:118948.
- [67] Zhang T, Murphy MJ, Yu H, Bagaria HG, Yoon KY, Neilson BM, et al. Investigation of nanoparticle adsorption during transport in porous media. *SPE J* 2015;20(04):667–77.
- [68] Rücker M, Bartels WB, Garfi G, Shams M, Bultreys T, Boone M, et al. Relationship between wetting and capillary pressure in a crude oil/brine/rock system: from nano-scale to core-scale. *J Colloid Interface Sci* 2020;562:159–69.
- [69] Edery Y, Berg S, Weitz D. Surfactant variations in porous media localize capillary instabilities during Haines jumps. *Phys Rev Lett* 2018;120(2):028005.
- [70] Liu F, Wang M. Trapping patterns during capillary displacements in disordered media. *J Fluid Mech* 2022;933:A52.